International Journal of Lightweight Materials and Manufacture 1 (2018) 179–188

Contents lists available at ScienceDirect

International Journal of Lightweight Materials and Manufacture

journal homepage: https://www.sciencedirect.com/journal/international-journal-of-lightweight-materials-and-manufacture

In-situ micro-tensile testing of AA2024-T3 fibre laser welds with digital image correlation as a function of welding speed

Joseph Ahn [a, *], Enguang He [b], Li Chen [b], John Dear [a], Zhutao Shao [a], Catrin Davies [a]

[a] Department of Mechanical Engineering, Imperial College London, South Kensington Campus, London, SW7 2AZ, UK
[b] Science and Technology on Power Beam Lab, Beijing Aeronautical Manufacturing Technology Research Institute, China

ARTICLE INFO

Article history:
Received 20 April 2018
Received in revised form
25 July 2018
Accepted 26 July 2018
Available online 1 August 2018

Keywords:
Aluminium alloy
Fibre laser welding
Digital image correlation
Joining
Microstructure

ABSTRACT

In this paper, the influence of welding speed on tensile properties of AA2024-T3 fibre laser welds was investigated by monitoring the deformation behaviour during tensile loading. In-situ micro-tensile testing combined with a high-resolution optical microscope and DIC was used to measure strain distribution in narrow weld regions showing characteristics of fibre laser beam welding with limited metallurgical modifications. A chemical etching technique was used to generate a micro-scale random speckle pattern by revealing the weld microstructure. Such pattern enabled a sufficient spatial resolution of strain while keeping the weld seam visible during deformation. The results of microstructural and mechanical properties determined under numerous welding speeds indicated that increasing the welding speed led to the transition of weld pool shape from circular to elliptical to teardrop with a greater fraction of equiaxed dendrites. The weaker strength of the weld, as measured by local lower micro-hardness values, constrained significant plasticity development locally within the weld. Tensile tests revealed that increasing the welding speed resulted in greater yield strength and ultimate tensile strength, whereas, total elongation to failure dropped. The tensile properties improved with increasing welding speed as the fraction of equiaxed dendrites increased.

1. Introduction

Aluminium alloy 2024-T3 is considered difficult to weld by fusion welding due to problems associated with cracking, poor weld appearance and defects such as porosity and undercut [1,2]. Alternative welding technique such as friction stir welding (solid state) is often used to achieve defect-free welds or use the conventional method of riveting instead to produce differential structures. However, these techniques cannot meet the increasing demands of high-capacity productions in the aircraft industry due to slow processing speed and limitations to producing high tolerance complex structures [3]. Recent developments in welding technologies have led to the innovative use of material forms and advanced joining methods such as high-power fibre laser beam welding to produce highly integrated structures [6], which are very effective in reducing weight and fabrication time and costs. The issues with integral welded structures, unlike differential riveted structures, are considerable changes in the microstructure, metallurgical state and associated material properties. For AA 2024-T3, the weld metal including the fusion zone (FZ) is the most critical region due to softening of the material after welding and so the integrity of the welded component is largely controlled by the weld seam [4–7].

Fibre laser welding is a relatively new welding process with a huge potential use in aircraft components as it offers significantly improved beam quality, output power and efficiency. Ahn et al. [1,2,8] showed that good quality defect-free fibre lased welded aluminium alloy 2024-T3 can be produced via parametric optimisation, yet the current lack of understanding of its tensile properties prevents the exploitation of their potential applications.

There are several techniques available for investigating the weld mechanical properties including micro-tensile testing of weld specimens extracted from the weld region, micro-hardness indentation testing, and testing of HAZ and FZ produced by Gleeble thermo-mechanical simulation. In this paper, a speckle patterning technique using chemical etching method was developed for Digital Image Correlation (DIC) analysis of local strains in

* Corresponding author.
E-mail address: joseph.ahn08@imperial.ac.uk (J. Ahn).
Peer review under responsibility of Editorial Board of International Journal of Lightweight Materials and Manufacture.

https://doi.org/10.1016/j.ijlmm.2018.07.003

the weld at a microscopic scale during an in-situ tensile test. Global and local strain and stress full fields in for the parent material, FZ and HAZ were determined using DIC. The resolution of the weld mechanical properties obtained was evaluated and discussed to optimise material performance.

Typically, a random speckle pattern as shown in Fig. 1 is applied on the specimen surface to perform DIC and measure displacements but covers the weld seam, making it difficult to accurately locate different regions within the weld during the test. In this investigation, the weld microstructure revealed by chemical etching was used instead as the speckle pattern to keep the microstructure visible. Such pattern did not have detachment problem which is frequently observed at high strains in typically applied speckle patterns [9] but also met the requirements of sufficient speckle size covering several grains, density and contrast to limit errors.

The influence of welding speed on weld tensile properties was investigated to find the optimum welding speed which maximises productivity while ensuring that welds meet quality standards. It is generally believed that a stronger weld strength can be achieved by welding using a fast welding speed, where a fine dendritic structure is promoted. On the other hand, it is also known that using a fast welding speed can lead to problems associated with hot cracking, where the fast solidification rate quickly induces thermal shrinkage strains, intensify rate of crack initiation and stress gradient, and shorten the time for residual melt along grain boundaries to sufficiently back-fill any crack [10]. Therefore, it was necessary in this investigation to identify the welding speed range upper limit to minimise the chance of forming transverse cracks due to the elongated temperature distribution in welding direction [11], as well as the lower limit to ensure that a sufficiently wide weld width can be obtained to lower crack sensitivity while keeping both the heat input and solidification rate low.

Fourteen samples were welded using various welding speeds and, one moderate and one high laser powers. The microstructural examination was conducted using standard sample preparation and imaging techniques. DIC was employed during in-situ micro-tensile testing to monitor the strain development.

2. Experimental procedures

2.1. Materials and process parameters

Al–Cu–Mg alloy 2024-T3 was used, where the T3 temper was obtained via solution treating, cold working followed by natural ageing at room temperature. The thickness of the sheet was 3.0 mm. An energy dispersive X-ray spectroscopy (EDX) was used to measure the chemical compositions at an accelerating voltage of 15 kV, an emission current of 76 μA, a working distance of 6.8 mm, an elevation of 35° and a live time of 50s as listed in Table 1.

A 5 kW Yb-fibre laser with a 300 μm processing fibre and 300 mm focal length, the focal beam size of 630 μm, Rayleigh length of 23 mm and beam parameter product of 2.50 mm mrad was used. Argon shielding gas was supplied from both front, side and root to completely shroud the melt pool. Table 2 lists the welding parameters selected to bead on plate weld with the results as shown in Fig. 2. Bead on plate welds were chosen over butt joints as they were easier to prepare and eliminated the need of accurate clamping and resulted in almost zero distortion. While there may be some differences between these two welding configurations, laser welding requires a very narrow gap tolerance matching the spot size even in butt joint configuration so specimen preparation for tensile test was easier in bead on plate configuration as the specimens were in a perfect geometry. It was ensured that the chosen processing parameters led to full penetration of the sheet to induce welding imperfections such as undercuts and reinforcements typically observed in butt joints. A constant focal position of 0 mm was used throughout the welding trials. The surface of the sheet was thoroughly cleaned chemically and mechanically ground using a steel wire brush to remove oxide layers and surface contaminants which are sources of porosity.

Fig. 1. Application of speckle pattern on weld tensile dog-bone sample surface.

Table 1
Chemical composition of AA2024-T3 (Wt. %).

Material	Al	Cu	Mg	Mn	Cr	Si
AA 2024-T3	91.9	5.9	1.2	0.6	0.1	0.3

Visual inspection was performed was performed to assess the surface appearance of the weld seams and levels of imperfections [12].

Weld sample preparation for the metallographic study was done by according to both ASTM E3 [13] and BS EN 1321 [14]. The polished specimens were chemically etched to reveal the weld microstructure. Keller's reagent was used by immersing the samples for 10 s. It was composed of 95% distilled water, 2.5% nitric acid, 1.5% hydrochloric acid and 1.0% hydrofluoric acid.

Inspection of weld cross-sections was performed according to BS EN 1321 [14]. The macroscopic inspection was done using 25× magnification, while microscopic examination was done using 50–500× magnification.

Micro-hardness was measured to assess the extent of weld softening in the FZ and HAZ according to ASTM E384 [15] as well as BS EN ISO-22826 [16]. A Zwick Z2.5 indenter was used with a load of 100 g and a hold period of 15 s at a rate of 60 μm/s selected to obtain the hardness profile across the sample.

Micro-tensile tests were also performed using a Deben in-situ dual lead screw micro-tensile testing stage with maximum loading to 2 kN and a cross-head speed of 0.2 mm/min controlled by a stepping motor. The tensile module was fitted to an optical microscope and the deformation during tensile testing was captured as digital images composed of 1600 × 1200 pixels every 0.5 s using the built-in Zeiss Axiocam microscope CCD camera at 50× magnification. An initial load of 1 N was applied to avoid the influence of any initial nonlinearity in the output of the miniature test. Miniature flat welded tensile samples with a width of 5.0 mm, the thickness of 0.4 mm and 8.0 mm gauge length as illustrated in Fig. 3, were wire cut from welded joints using electrical discharge machining (EDM).

2.2. Digital image correlation

In-situ micro-tensile tests were performed using the DIC system to analyse the evolution of strain field during loading and to obtain the mechanical properties of welded specimens. The small and varied size of different microstructural regions of the weld makes it difficult to accurately determine the local mechanical properties from standard tensile specimens. Also, as the plastic strain distribution in the standard tensile specimen is inhomogeneous over the gauge length, the tensile properties are highly dependent on the chosen gauge length at which they were measured [17,18]. The advantage of using chemically etched micro-tensile specimens was that it was possible to obtain a close view of the entire weld zone at high magnifications and resolution and also observe the

Table 2
Parameters for autogenous laser beam welding with different welding speed and laser power.

Sample Number	Laser Power (kW)	Travel Speed (m/min)	Power Density (MW/cm^2)	Total Heat Input (J/mm)
V-1-1	4.5	5.1	2.83	0.88
V-1-2	4.5	4.5	2.83	1.00
V-1-3	4.5	3.9	2.83	1.15
V-1-4	4.5	3.3	2.83	1.36
V-1-5	4.5	2.7	2.83	1.67
V-1-6	4.5	2.1	2.83	2.14
V-1-7	4.5	1.5	2.83	3.00
V-2-1	3.0	5.1	1.89	0.59
V-2-2	3.0	4.5	1.89	0.67
V-2-3	3.0	3.9	1.89	0.77
V-2-4	3.0	3.3	1.89	0.91
V-2-5	3.0	2.7	1.89	1.11
V-2-6	3.0	2.1	1.89	1.43
V-2-7	3.0	1.5	1.89	2.00

deformation directly from the clearly visible etched FZ and HAZ without the need to apply speckle patterns on their surfaces. The difficulties in accurately measuring strain in the micro-tensile specimens due to their limited size were solved by using the DIC which allowed determining both global and local strain field of each individual regions from the examined surface area.

To optimise the resolution of DIC images, the facet step was chosen to be a quarter of the facet size to make adjacent facets overlap. Each facet centre was assigned x and y coordinates and characterised by a grey scale distribution. The facets of the initial image were matched to positions in successive images after loading to obtain displacement vector for all points in the specimen. Full field displacement data was then obtained. Cross-correlation was used to identify the movement of the speckle pattern from an image series and determined the deformation strains and vectors. The algorithm measured full-field displacements by searching for the best correlation between subsets, which was defined in the reference image. Optimisation techniques were used to find its best match in the deformed image and repeating this process gave the displacement field.

3. Results and discussion

3.1. Speckle pattern and microstructure

Variations in macrostructures of weld surfaces with welding speed are shown in Fig. 4. The weld pool size, shape and solidification pattern were controlled by the heat transfer in the vicinity of the molten pool and the nature of the molten pool fluid motion [19]. Other than thermo-physical properties of the material, welding speed and heat input significantly influenced the solidification behaviour of the welds. The formation of dendrites in the weld including its shape and size varied according to steep thermal gradients and rapid solidification rates. The welding speed affected the alignment of grains, where high speed led to lower local melt flow rate and temperature gradient within the weld pool and faster solidification or cooling rate. A finer dendritic solidification microstructure was formed by raising the speed.

Fig. 4 shows the effect of welding speed on weld solidification microstructure. The arrows inside the weld pool indicate the direction of grain alignment during solidification. At a slow welding speed of 1.0 m/min, a circular pool shape with similar leading (melting) and trailing (solidifying) end shapes was observed as shown in Fig. 4 (a). Also, both circular and straight ripple marks (solidification front) were found at the weld centreline. The solidifying grains grew from the fusion line towards the centre of the weld, with the solidifying ends (arrow) being perpendicular to the melt pool boundary (circle). At 2.1 m/min, the molten pool became elongated and elliptical with the long axis parallel to the welding direction, with V-shaped ripple marks and grains growing perpendicular to the elongated pool boundary. At 3.9 m/min, the weld pool became tear-drop shaped with a long tail and the grains grew almost perpendicular to the welding direction.

The solidification microstructure was controlled by a temperature gradient (G) and solidification rate (R), where G/R determined the solidification mode and the G·R determined the grain size and morphology [20]. The grain morphology changed from planar and cellular dendritic at the fusion line G/R was relatively high, to columnar dendritic and equiaxed dendritic towards the weld centreline where G/R became lower. Increasing the welding speed resulted in a lower thermal gradient but a faster cooling rate due to the drop in the total heat input and peak temperature in the weld

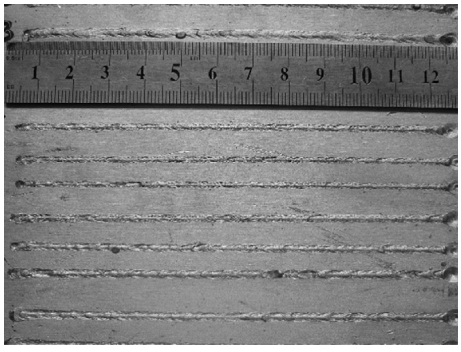

Fig. 2. Autogenous bead on a plate welded AA2024-T3 of different welding speeds.

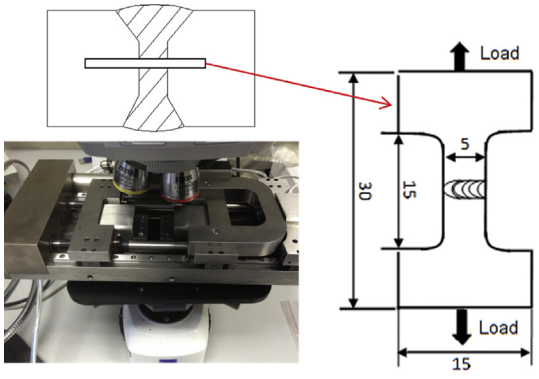

Fig. 3. Micro-tensile specimens extracted from the mid-section of a weld seam and mounted on a micro-tensile testing rig under an optical microscope.

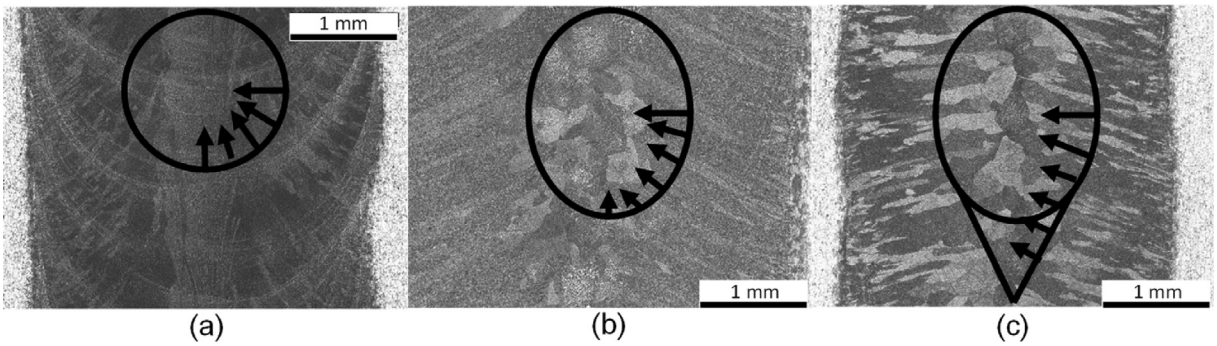

Fig. 4. Effect of changing speed on weld surface appearance and weld solidification microstructure showing flow patterns at (a) 1.0 m/min, (b) 2.1 m/min and (c) 3.9 m/min given 4.5 kW.

pool surface, so G·R increased but G/R decreased. Hence, the formation of a fine dendritic structure with smaller dendritic arm spacing was promoted at faster welding speed.

As Fig. 5 (a) and (d) shows, the solidification front is planar along the fusion line and transforms to columnar dendritic as the weld centreline is approached as shown in Fig. 5 (c). The weld centre was dendritic with both equiaxed fine columnar grains as shown in Fig. 5 (b). The number of equiaxed dendrites increased with increasing speed. Increasing the speed promoted a fine dendritic structure and grain sizes due to constitutional super-cooling resulting from a low G/R. The columnar grains growth was epitaxial at faster speeds. On the other hand, at lower speeds, the columnar dendrites curved away from the perpendicular to the welding direction and aligned parallel to the direction of heat flow. The measured HAZ width was less than 0.1 mm due to the steep temperature gradient, low heat input and rapid solidification rate which were characteristics of fibre laser beam welding with limited metallurgical modifications.

Figs. 6 and 7 show the welded micro-tensile specimens after chemical etching loaded on the micro-tensile stage. The observed weld width decreased with increasing speed, where slow speed led to high heat input and wide weld width. The bottom reference images show the weld surfaces overlaid with initial blue facet elements (matrix of pixels) containing several grain variations, assigned by the DIC software to allow determination of displacement and strain in a plane parallel to the image plane of the optical microscope. The use of etched microstructural features as random speckle pattern allowed accurate monitoring of strain evolution in different microstructural regions of the weld.

3.2. Full field strain mapping during tensile testing

The displacement and strain fields for each specimen was determined by capturing multiple images during deformation and through subsequent analyses. The resulting strain field parallel to the tensile axis for specimens of different welding speeds just

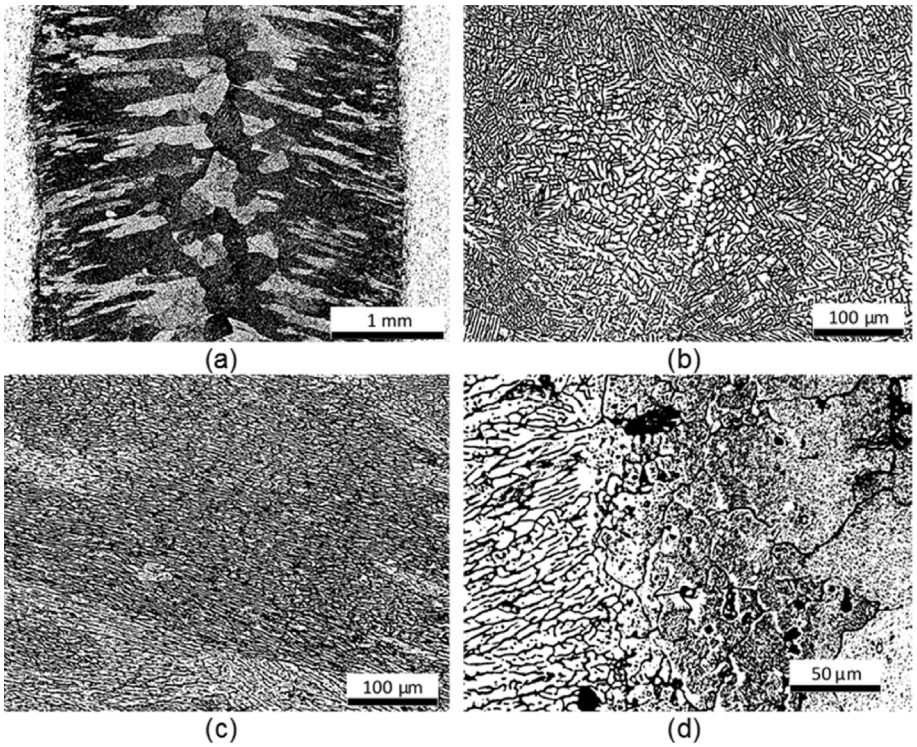

Fig. 5. Microstructure of fibre laser welded AA2024-T3 processed given 3.0 kW and 3.9 m/min showing (a) weld seam 25×, (b) equiaxed dendrites in FZ 200×, (c) columnar dendrites in FZ 200× and (d) HAZ 500×

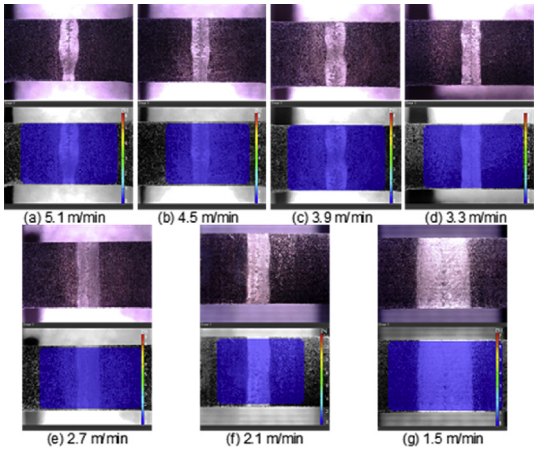

Fig. 6. Chemically etched welded micro-tensile specimens processed using various welding speeds given 4.5 kW at the beginning of the tensile test and DIC facet elements in the reference image determined on the etched microstructure.

before rupture during the tensile test is shown in Figs. 8 and 9 for the laser power of 4.5 and 3.0 kW, respectively. To maximise contrast, the lower and upper limits of the colour scales for each welding speed was chosen independently. While the 2D DIC technique allows calculation of all three in-plane strain components, the contributions from shear strain and the strain component perpendicular to the tensile axis was negligible.

Throughout the test, the strain was confined to the FZ, clearly revealing higher localised strain than the surrounding parent material where the blue contour indicates mostly elastic strain during the test, at all speeds. This was due to localised strains in softened weld zone resulting in a relatively low ductility. The size of the localised strain region as illustrated by the strain contour map in red, became enlarged with increasing speed. A gap in the strain map as shown in Fig. 9 (c) was caused by excessive levels of plastic deformation, where cracks started growing in the FZ, thus distorting the subset geometry and preventing from tracking the subsets in the subsequent image series. A trend was found where the peak strain reached in the FZ prior to failure dropped with increasing speed. At lower speed, columnar dendrite growth was preferred and reduced the likelihood of forming equiaxed dendrites, resulting mostly in columnar dendritic structure and the

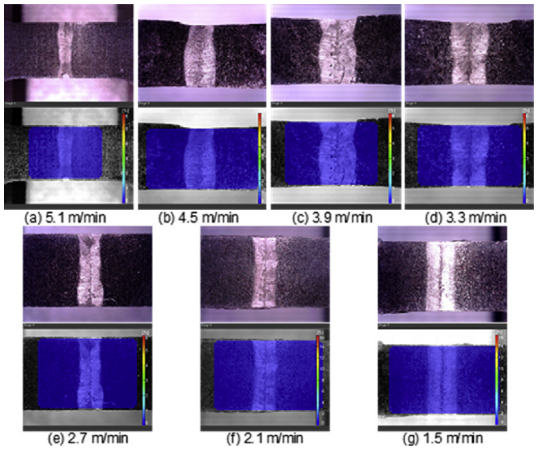

Fig. 7. Chemically etched welded micro-tensile specimens processed using various welding speeds given 3.0 kW at the beginning of the tensile test and DIC facet elements in the reference image determined on the etched microstructure.

weld width became wider. A wider weld pool size reduced the risk of solidification cracking and decreased the stress levels across the weld seam during solidification. On the other hand, the maximum strain decreased from around 14%–7% when reducing the speed from 2.1 to 1.5 m/min, given 4.5 kW, where the total heat input increased from 2.15 to 3.00 J/mm so the excessive heat input at 1.5 m/min had a negative effect on the ductility. Such phenomenon was not observed at the same speeds given 3.0 kW as expected because the total heat input was equal to 1.45 and 2.00 J/mm at 2.1 and 1.5 m/min, respectively, which were less than 3.00 J/mm so the maximum strain reached at these two welding was similar, of around 16%. For both laser powers, the lowest maximum strain was measured at 5.1 m/min. These results were in close agreement with the findings of Ahn et al. [21] who reported that centreline solidification cracking was observed above a total heat input of 2.5 J/mm for fibre laser welded 3.0 mm thick AA 2024-T3 sheets, as a result of excessive heat input in the molten weld pool, where more molten material led to larger contraction strain and caused larger cracks to form. In addition, reduced solidification rate due to increased total heat input caused impurity elements to diffuse into the molten pool and the resulting weakened weld microstructure become more susceptible to cracking. On the other hand, power density of less than 1.2 MW/cm^2 and total heat input of less than 1.0 J/mm resulted in incomplete penetration. According to Janasekaran et al. [22], who examined the effect of low power laser welding with total heat input values ranging between 0.2 and 0.4 J/mm, the pull force required to fracture T-joint welded specimens increased with decreasing welding speed from 21 mm/s to 12 mm/s. Such trend was caused by the lower heat input at faster welding speed, which reduced the width of the FZ, the depth of penetration and decreased the amount of smaller grains in the FZ and therefore, increased the ductility by allowing larger amounts of slip to occur.

3.3. Fracture behaviour

Fractography on micro-tensile specimens revealed that cracks initiated and fractured in the FZ as depicted in Figs. 10 and 11. Unlike the unwelded parent material which underwent significant necking before failure, the welded specimens failed with much less macroscopic necking in the FZ. At high welding speed, the fracture path was jagged with several cracks growing parallel to the tensile axis, following the grain growth direction and ripple marks perpendicular to the welding direction. Hence, a mixed failure mode including the weld centreline as well as the fusion line was observed. The cracks propagated towards the fusion boundary where the property gradient was the steepest. Increased welding speed resulted in a fine grain size by limiting grain growth and narrow weld width which increased the stress levels across the weld seam during solidification but minimised microstructural modification or loss of strength by melting or coarsening of precipitates in HAZ and reduced low boiling point alloying element evaporation due to increased cooling rate and reduced time exposed to peak temperatures for grain coarsening [23]. Microcracks were observed on the fracture surface along equiaxed grain boundaries at high welding speed which was assumed to be solidification cracks which tend to form at high welding speed. At low welding speed, the strain was concentrated in the columnar dendrites and failed in this region.

3.4. Mechanical properties

For each sample, the strain distribution near the laser weld at different times during the tensile test was found as shown in Figs. 12 and 13. The strains displayed significant heterogeneities in strain distribution across the weld, indicating the transition from

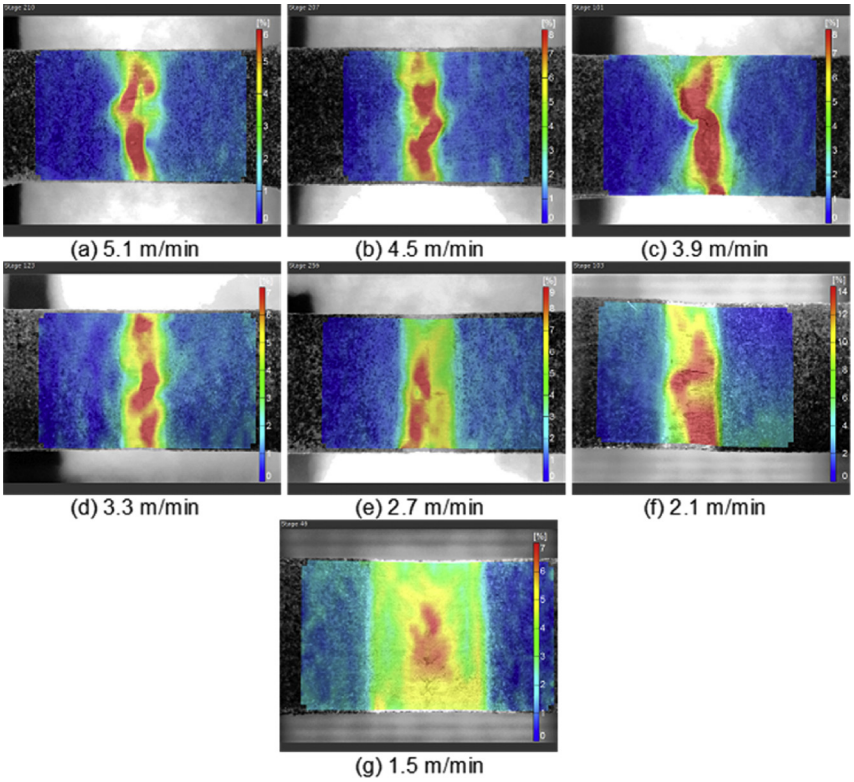

Fig. 8. 2D DIC full field axial strain maps for various speeds given 4.5 kW at the onset of fracture.

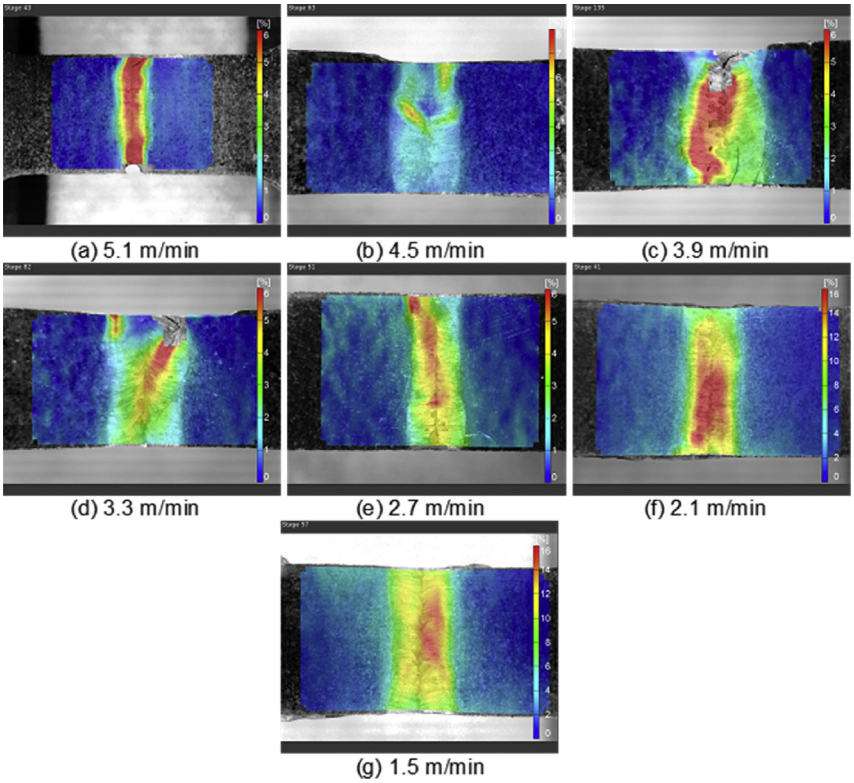

Fig. 9. 2D DIC full field axial strain maps for various speeds given 3.0 kW at the onset of fracture.

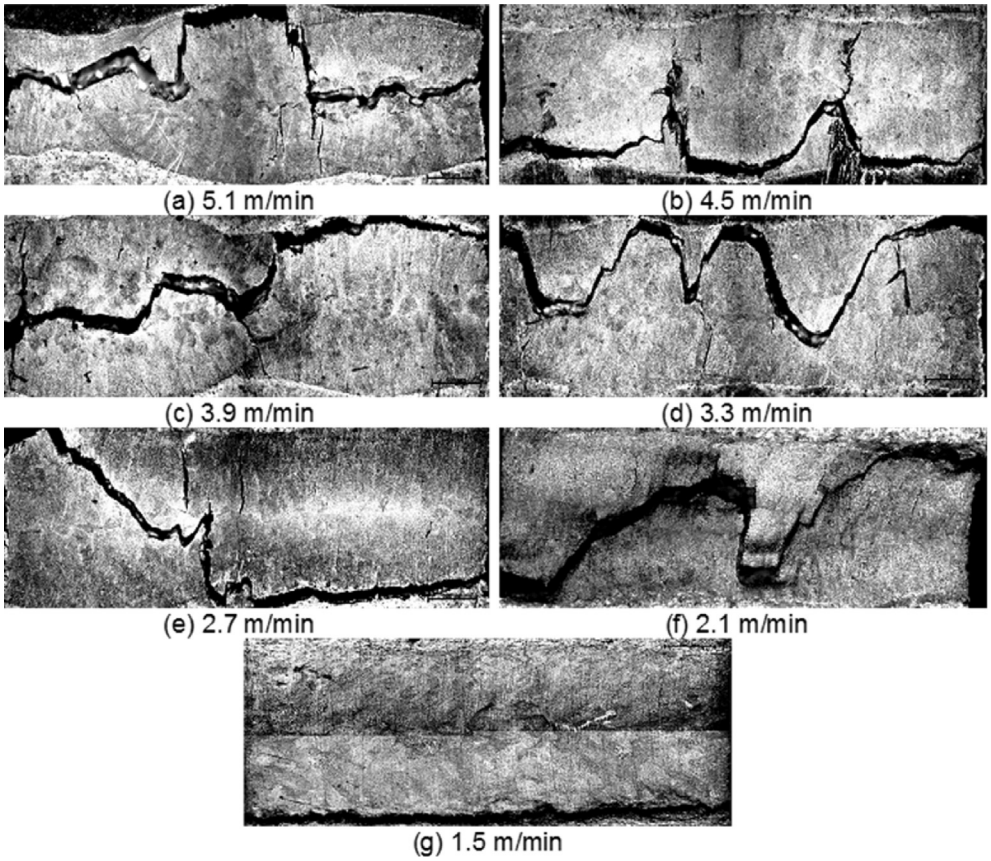

Fig. 10. Micrograph of fractured micro-tensile weld specimens showing the failure location and behaviour for various speeds given 4.5 kW.

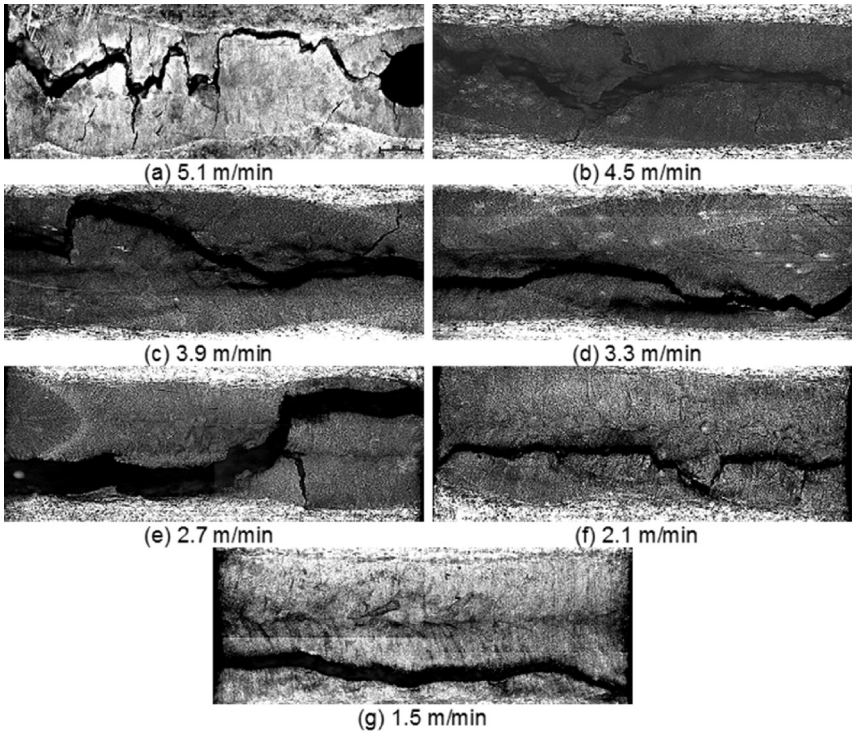

Fig. 11. Micrograph of fractured micro-tensile weld specimens showing the failure location and behaviour for various speeds given 3.0 kW.

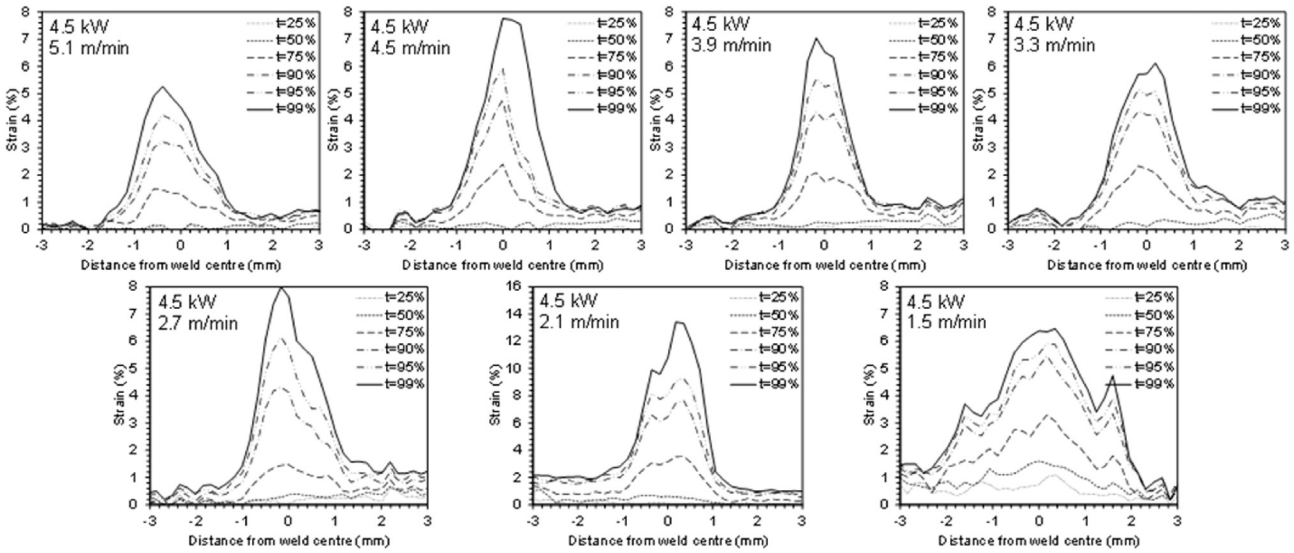

Fig. 12. Development of local axial strain distribution across the weld seam relative to the failure time for various speeds given 4.5 kW.

parent material to HAZ to FZ. The failure strain values at 99% of the time to failure was relevant in the FZ where the failure took place and served as the lower limit for the HAZ and the parent material. Therefore, the weaker strength of the FZ reduced plasticity development within the weld. Strain localisation in the FZ meant that the full plastic deformation in the other regions was precluded when the least ductile FZ failed to result in a comparatively low overall macroscopic strain so it was possible that these regions had greater ductility than the FZ. As mentioned above, the strain value in the unaffected parent material was typically less than 2% showing that the material was still under elastic loading, whereas, the total strain reached at least 6% and up to 16% in the FZ prior to failure. The maximum local plastic strain distribution within the weld was found to decrease with increasing welding speed from above 14% at 2.1 m/min to around 5% at 5.1 m/min. Increasing the speed reduced the heat input and caused the finer dendritic structure to form with a higher equiaxed ratio and grain sizes in the FZ.

The true constitutive behaviour of different microstructural regions of transverse weld specimens, including the softened local FZ and the HAZ surrounded by the BM, were determined by assuming the weld as a composite material deforming under an iso-stress condition and property gradients are not huge. By matching the localised strain field obtained using the DIC with the remotely applied global load, it was possible to determine the local stress-strain response in the FZ and the HAZ as there was no uncertainly regarding whether the selected tensile data was representative of the material in the weld. The local strain value was calculated in the FZ, HAZ as well as globally from hundreds of time steps. The observed stress and strain response for different welding speeds are shown in Figs. 14 and 15. As expected, strain localisation occurred at the weakest component of the composite material loaded in an iso-stress configuration, which was the weld seam.

The softened weld zone clearly displayed a very different response compared to the parent material, where on average the FZ had a 0.2% proof stress of less than 250 MPa for a range of welding speeds, which was much lower than the parent of around 390 MPa as shown in Fig. 16. At fast welding speed, the strain was lower than 0.2% plastic strain in the HAZ and overall, indicating that the local

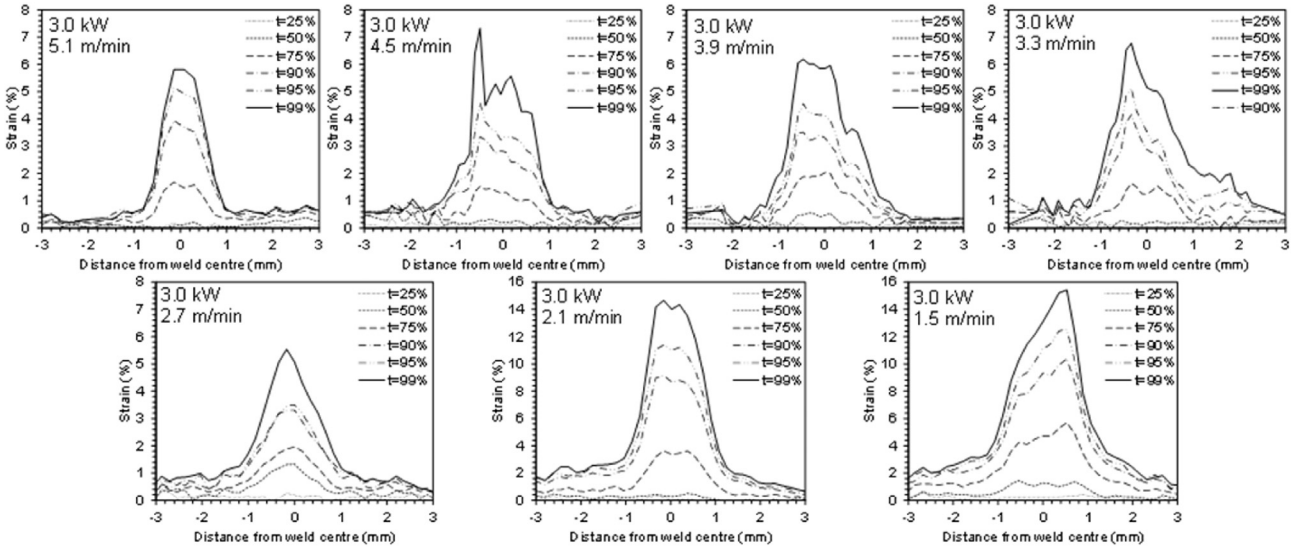

Fig. 13. Development of local axial strain distribution across the weld seam relative to the failure time for various speeds given 3.0 kW.

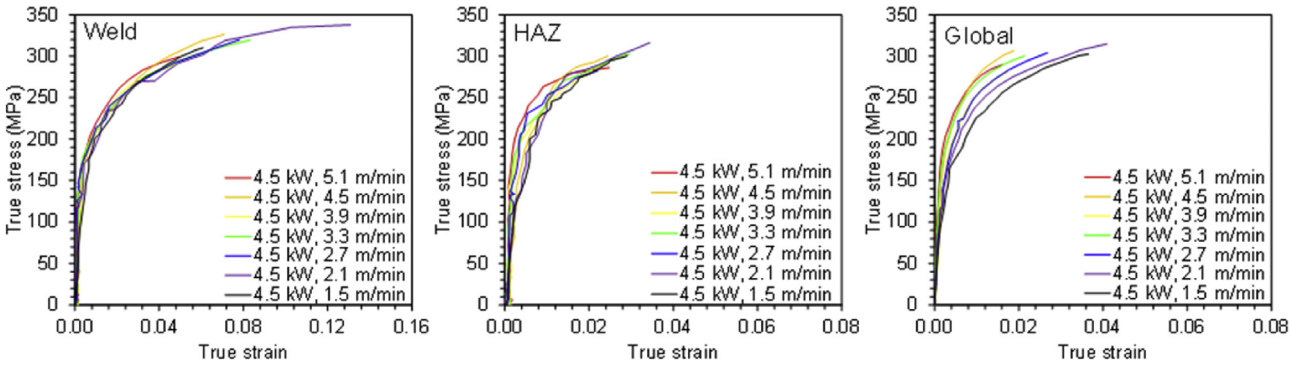

Fig. 14. Local and global constitutive properties of welded samples including FZ and HAZ determined with DIC method for various speeds given 4.5 kW.

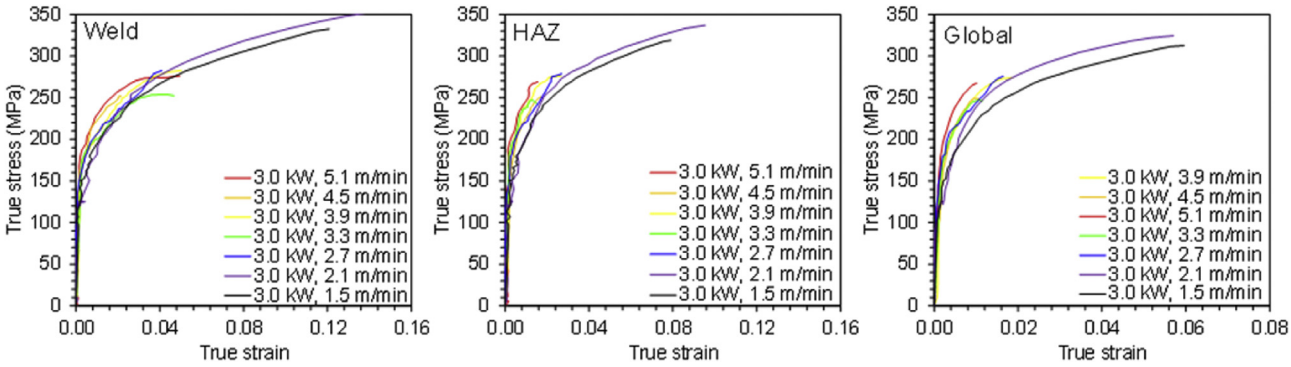

Fig. 15. Local and global constitutive properties of welded samples including FZ and HAZ determined with DIC method for various speeds given 3.0 kW.

FZ yield strength was considerably greater compared to the global failure stress. The results show that the use of conventional tensile testing with a macroscopic extensometer would be incapable of discerning the difference in material behaviour between the weld and the parent. It is interesting to note that grain growth was limited at high speed so the YS and UTS increased with increasing speed, whereas, ductility decreased. As the fraction of equiaxed dendrites became greater with increasing speed, the weld tensile properties at the cost of reduced plasticity.

Dissolution of strengthening precipitates by welding resulted in its softening and the effect was more pronounced in the FZ than the HAZ due to higher temperatures experienced and so a greater dissolution of strengthening phases occurred as a consequence [4,5,24]. Fig. 16 (a) shows a large difference in stress and strain behaviour between the weld metal and the parent material. A considerable loss of yield and tensile strength to around 60% as well as global ductility to 30% was observed due to strain localisation in the softened FZ which led to premature failure. However, a similar ductility to the parent material was recorded in the localised FZ, with the highest value of around 0.16 at 2.1 m/min for both laser powers.

Fig. 16 (b) illustrates the typical transverse micro-hardness profile across the weld seam at mid-thickness produced using a

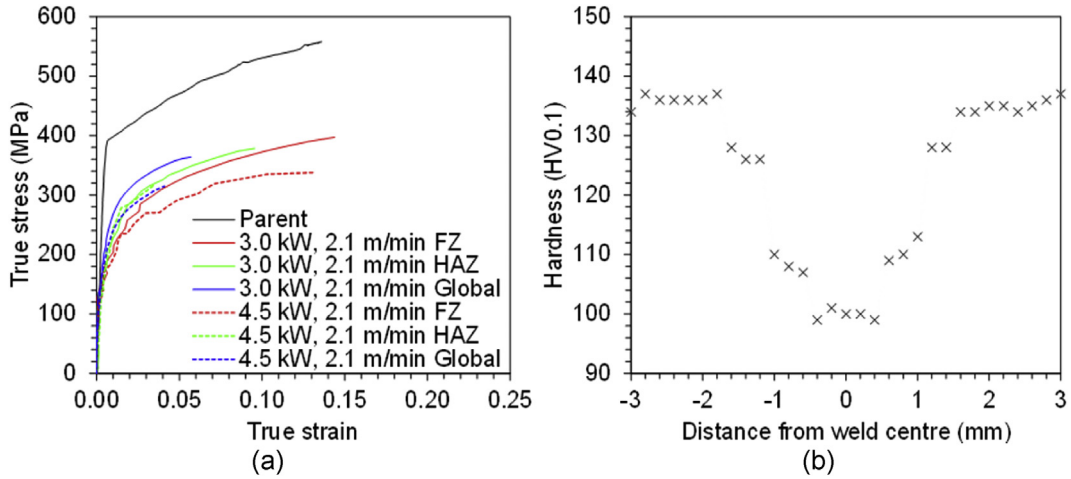

Fig. 16. (a) Stress and strain response of welded versus unwelded tensile specimen and (b) micro-hardness distribution profile for the AA 2024-T3 weld exhibiting softening in the weld metal (power 4.5 kW, speed 2.1 m/min, focused beam).

laser power of 4.5 kW and a welding speed of 2.1 m/min. The distinct degradation of micro-hardness in the FZ of less than 100 HV and 110–120 HV in the HAZ compared to over 130 HV in the parent material was due to loss of strength (softening) in the FZ when exposed to high temperatures during welding and subsequent change in weld solidification microstructure due to dissolution of precipitates. It was also possible that the change in weld chemical composition due to vaporisation of low boiling point alloying elements, especially magnesium during welding at laser high power density, contributed to the lower hardness. The T3 temper after welding in the FZ corresponded to the as-fabricated fully annealed and soft condition, since no temperature control was performed during and after welding for solution heat treatment and natural ageing.

4. Conclusions

Troubles in monitoring local strains due to the small size of different microstructural regions of AA 2024-T3 fibre laser welds was solved by using digital image correlation with chemical etching method to create random speckle pattern for in-situ micro-tensile testing on miniature specimens. The etched weld microstructure had a high-quality pattern with good spatial resolution and allowed precise measurement of local strain variations to relate them with microstructural heterogeneities within the weld.

Welding speed influenced the alignment of grains, where increasing it led to lower local melt velocity and thermal gradient in the weld pool and faster solidification rate. The grain morphology changed from planar and cellular dendritic at the fusion line where the ratio of G and R was relatively high, to columnar dendritic and equiaxed dendritic towards the weld centreline where the ratio became lower.

The maximum strain dropped with increasing speed from around 16%–7%, whereas, at a very low speed of 1.5 m/min, the resulting excessive heat input had a negative effect on the ductility. The weaker strength of the weld constrained plasticity development locally within the fusion zone.

Tensile tests revealed that the YS and UTS increased with increasing speed, whereas, total elongation to failure decreased. As the fraction of equiaxed dendrites increased with increasing speed, the weld tensile properties improved. The optimum processing condition within the investigating domain was therefore, found at a welding speed of 2.1 m/min, both for the laser power of 3.0 and 4.0 kW, where a sufficiently low welding speed and heat input (or laser power) was obtained to lessen the effect of solidification cracking.

References

[1] J. Ahn, L. Chen, E. He, C.M. Davies, J.P. Dear, Effect of filler metal feed rate and composition on microstructure and mechanical properties of fibre laser welded AA 2024-T3, J. Manuf. Process. 25 (2017) 26–36, https://doi.org/10.1016/j.jmapro.2016.10.006.
[2] J. Ahn, E. He, L. Chen, J. Dear, C. Davies, The effect of Ar and He shielding gas on fibre laser weld shape and microstructure in AA 2024-T3, J. Manuf. Process. 29 (2017), https://doi.org/10.1016/j.jmapro.2017.07.011.
[3] J. Enz, M. Kumar, S. Riekehr, V. Ventzke, N. Huber, N. Kashaev, Mechanical properties of laser beam welded similar and dissimilar aluminum alloys, J. Manuf. Process. 29 (2017) 272–280, https://doi.org/10.1016/j.jmapro.2017.07.030.
[4] V. Alfieria, F. Caiazzoa, V. Sergi, Autogenous laser welding of AA 2024 aluminium alloy: process issues and bead features, Procedia CIRP 33 (2015) 406–411, https://doi.org/10.1016/j.procir.2015.06.094.
[5] F. Caiazzo, V. Alfieri, F. Cardaropoli, V. Sergi, Butt autogenous laser welding of AA 2024 aluminium alloy thin sheets with a Yb:YAG disk laser, Int. J. Adv. Manuf. Technol. 67 (2013) 2157–2169, https://doi.org/10.1007/s00170-012-4637-7.
[6] J. Ahn, L. Chen, C.M. Davies, J.P. Dear, Digital image correlation for determination of local constitutive properties of fibre laser welding joints in AA2024-T3, in: Proc. 16th Int. Conf. Exp. Mech., University of Cambridge, Cambridge, GB, 2014, pp. 1–2.
[7] J. Ahn, E. He, L. Chen, R.C. Wimpory, S. Kabra, J.P. Dear, et al., FEM prediction of welding residual stresses in fibre laser-welded AA 2024-T3 and comparison with experimental measurement, Int. J. Adv. Manuf. Technol. 95 (2018), https://doi.org/10.1007/s00170-017-1548-7.
[8] L. Chen, E. He, J. Ahn, J. Dear, Parametric optimization and joint heterogeneity characterization of fiber laser welding of AA2024-T3, in: Proc. 67th Annu. Assem. Int. Inst. Weld., International Institute of Welding, Seoul, KR, 2014, pp. 1–9, https://doi.org/10.13140/RG.2.2.25784.96005.
[9] M. Segolle, J. Santos, K.A. Kasvayee, A.E.W. Jarfors, Etching method to create a random speckle pattern on semi-solid cast A356 aluminium for DIC in-situ strain measurements, J. Cast. Mater. Eng. 1 (2017) 33, https://doi.org/10.7494/jcme.2017.1.1.33.
[10] X. Cao, W. Wallace, J.-P.P. Immarigeon, C. Poon, Research and progress in laser welding of wrought aluminum alloys. II. Metallurgical microstructures, defects, and mechanical properties, Mater. Manuf. Process. 18 (2003) 23–49, https://doi.org/10.1081/AMP-120017587.
[11] B. Hu, I.M. Richardson, Mechanism and possible solution for transverse solidification cracking in laser welding of high strength aluminium alloys, Mater. Sci. Eng. 429 (2006) 287–294, https://doi.org/10.1016/j.msea.2006.05.040.
[12] BS EN ISO 15614-11:2002 Specification and qualification of welding procedures for metallic materials — Welding procedure test — Part 11 Electron and laser beam welding n.d.
[13] ASTM E3 Methods for Preparation of Metallographic Specimens n.d.
[14] BS Standard EN ISO 17639:2013, “Destructive tests on welds in metallic materials. Macroscopic and microscopic examination of welds”, BSI, 2013 n.d.
[15] ASTM E384 Standard Test Method for Micro-indentation Hardness of Materials n.d.
[16] BS ISO 22826:2005 Destructive tests on welds in metallic materials. Hardness testing of narrow joints welded by laser and electron beam (Vickers and Knoop hardness tests) n.d.
[17] R.M. Molak, K. Paradowski, T. Brynk, L. Ciupinski, Z. Pakiela, K.J. Kurzydlowski, Measurement of mechanical properties in a 316L stainless steel welded joint, Int. J. Pres. Ves. Pip. 86 (2009) 43–47, https://doi.org/10.1016/j.ijpvp.2008.11.002.
[18] M. Koçak, J. dos Santos, S. Riekehr, Trends in laser beam welding technology and fracture assessment of weld joints, Sci. Technol. Weld. Join. 6 (2001) 347–350, https://doi.org/10.1179/136217101322910498.
[19] R. Trivedi, S.A. David, M.A. Eshelman, J.M. Vitek, S.S. Babu, T. Hong, et al., In situ observations of weld pool solidification using transparent metal-analog systems, J. Appl. Phys. 93 (2003) 4885–4895, https://doi.org/10.1063/1.1559934.
[20] D. Sen, M.A. Pierson, K.S. Ball, Coupled field analysis of a gas Tungsten arc welded butt joint—part II: parametric study, J. Therm. Sci. Eng. Appl. 6 (2013) 21009, https://doi.org/10.1115/1.4024704.
[21] J. Ahn, L. Chen, E. He, J.P. Dear, C.M. Davies, Optimisation of process parameters and weld shape of high power Yb-fibre laser welded 2024-T3 aluminium alloy, J. Manuf. Process. 34 (2018) 70–85, https://doi.org/10.1016/j.jmapro.2018.05.028.
[22] S. Janasekaran, M.F. Jamaludin, M.R. Muhamad, F. Yusof, M.H. Abdul Shukor, Autogenous double-sided T-joint welding on aluminum alloys using low power fiber laser, Int. J. Adv. Manuf. Technol. 90 (2016) 3497–3505, https://doi.org/10.1007/s00170-016-9677-y.
[23] G. Padmanabham, B. Shanmugarajan, Experimental investigation of bead-on-bead CO2 laser welding of Al alloy 6061, in: S.A. David, T. DebRoy, J.N. DuPont, T. Koseki, H.B. Smartt (Eds.), Trends Weld. Res. 2008 Proc. 8th Int. Conf., ASM International, Pine Mountain, GA, 2009, pp. 598–603, https://doi.org/10.1361/cp2008twr598.
[24] V. Alfieri, F. Caiazzo, F. Cardaropoli, V. Sergi, Issues in disk-laser key-hole welding of 2024 aluminum alloy, Front Aerosp Eng 1 (2012) 36–44.